International Journal of Coal Geology 225 (2020) 103496

Contents lists available at ScienceDirect

International Journal of Coal Geology

journal homepage: www.elsevier.com/locate/coal

Swelling and embedment induced by sub- and super-critical-CO_2 on the permeability of propped fractures in shale

Lei Hou[a,*], Derek Elsworth[b,*], Xueyu Geng[a]

[a] School of Engineering, The University of Warwick, Coventry CV4 7AL, UK
[b] Energy and Mineral Engineering, EMS Energy Institute and G3 Center, Pennsylvania State University, University Park 16802, USA

ARTICLE INFO

Keywords:
Swelling
Embedment
Propped shale fracture
Permeability
Carbon dioxide

ABSTRACT

Swelling and embedment exert significant influence on the evolution of permeability in propped fractures, potentially consuming significant proportions of the original gain in permeability. We measure the evolution of permeability in propped fractures of shale to both adsorbing CO_2 and non-adsorbing He – accommodating the impacts of aperture change due to proppant pack compaction and both reversible and irreversible modes of embedment. A linear relation between pressure and log-permeability is obtained for He, representing the impact of effective stresses in proppant pack compaction, alone. Permeability change with pressure is always concave upwards and U-shaped for gaseous subcritical CO_2 and W-shaped for supercritical CO_2. One exception is for liquid CO_2 at high injection pressure where effective stress effects and swelling contribute equally to the change in permeability and result in a linear curve with the lowest permeability. Approximately ~50–70% of the permeability recovers from the recovery of swelling after the desorption of CO_2. The magnitude of swelling is recovered from measurements of permeability change and ranges from 0.005 to 0.06 mm, which contributes ~9–56% of the total swelling and induced embedment as evaluated from the adsorbed mass. Swelling also increases embedment by a factor of ~1.84–1.93 before and after the injection of CO_2. A new calibration equation representing swelling and induced embedment is generated accommodating Langmuir isothermal sorption and verified against experiments on rocks both admitting and excluding swelling and embedment and for various sorbing and non-sorbing gases. Stability and accuracy of the predictions demonstrate the universality of the approach that may be applied to both enhanced gas recovery and CO_2 sequestration.

1. Introduction

CO_2 applications have a long history in the energy industries including for EOR (Enhanced Oil Recovery) (Kolster et al., 2017; Wang et al., 2015), CO_2 fracturing (Liu et al., 2014; Middleton et al., 2015; Xinwei Zhang et al., 2017) and for storage in saline aquifers and depleted reservoirs (Bielicki et al., 2018; Buscheck et al., 2016; Tayari and Blumsack, 2020). As a strongly adsorbing gas, permeability evolution involving swelling and fracture closure is one essential issue. Sorbing CO_2 swells the rock matrix and causes a reduction in the natural fracture aperture (Liu and Rutqvist, 2009; Mazumder and Wolf, 2008; Zhang et al., 2019). This swelling behaviour follows the Langmuir isotherm and reaches maximum influence at approximately twice the Langmuir pressure (Wang et al., 2011). The competition between swelling and effective stress results in a typical U-shaped curve for permeability as a function of increasing gas pressure for both integral and split samples (Kumar et al., 2015; Wang et al., 2013). Where the fluid is supercritical, a W-shaped curve may additionally result (Zhi et al., 2019).

An accompanying issue with a similar significant impact on permeability is that of particle embedment in propped fractures - occurring when the particle has a higher stiffness than the rock. The embedment, by itself, may induce a 10 to 60% reduction in fracture aperture with a subsequent significant (78%) loss in conductivity in shale (Bandara et al., 2019; Santos et al., 2018; Zhang and Hou, 2016). Prior characterizations have examined the roles of mineral composition (clay content), mechanical properties, interaction between the rock surface and the fracturing fluid, closure stress, proppant concentration and formation temperature and pressure in modulating response (Arshadi et al., 2017; Tang and Ranjith, 2018; Wen et al., 2007; Zhang et al., 2015). Swelling is relatively less important for shales, relative to coals, because of their lower organic contents and higher stiffnesses. However, conventional methods of characterization applied in former studies are incapable of distinguishing between swelling and embedment

* Corresponding authors.
E-mail addresses: lei.hou@warwick.ac.uk (L. Hou), elsworth@psu.edu (D. Elsworth).

https://doi.org/10.1016/j.coal.2020.103496
Received 24 February 2020; Received in revised form 24 April 2020; Accepted 24 April 2020
Available online 01 May 2020

under either static loading or API (American Petroleum Institute) standard conductivity tests. Associated with swelling, embedment is accentuated in rocks of low modulus. Recent studies have demonstrated the significant effect of swelling on permeability evolution in propped fractures in shale which are also shown to result in typical U-shaped curves of permeability with pressure (Li et al., 2017).

Nonetheless, the behaviour of swelling and induced embedment, and their respective contribution to the destruction of permeability in propped fractures, is poorly defined since the direct observation of swelling is infeasible in real-time and under triaxially stressed, sealed and gas injection conditions. Therefore, we explore the impacts of swelling-induced embedment of proppant in artificial fluid-driven fractures. We measure permeability loss with the injection of both non-adsorptive Helium (He) and adsorptive carbon dioxide (CO_2) on samples of Green River shale to (i) quantitatively reveal the respective roles of swelling and embedment, (ii) define the different controlling mechanisms of permeability evolution, and (iii) define a model for embedment that accommodates the influence of swelling that provides a better prediction of fracture conductivity and understanding of gas production and CO_2 sequestration.

2. Methodology

We measure permeability evolution to CO_2 and He in propped fractures in both shale (that accommodates embedment and swelling) and granite (that excludes these effects) via pressure transient (pulse) methods. The apparatus (core holder and reservoirs) is immersed within a temperature-controlled water bath to control the state of CO_2, as either sub- or super-critical. We measure permeability to CO_2 and He alternately in the same sample. Based on the outcomes, we define controlling mechanisms on the evolution of embedment and their impact on permeability.

2.1. Materials and preparation

Axially-split core samples (25 mm diameter 50 mm length) of Westerly granite and Green River shale are placed in a pressurized core holder with proppant sandwiched within the fracture. The high strength Carbo-Lite ceramic proppant is segregated by size fraction (40/80 mesh). A single layer of proppant is first sandwiched between the two facing artificial fractures. In particular, we explore the behaviour of a monolayer since the deformation of proppant can be calculated more accurately, and leaves swelling and embedment as the main factors influencing permeability evolution. The proportion of monolayer-propped fractures in field-fracturing is significant. This is apparent in branch fractures or micro-fractures and composes a crucial amount of the total stimulated reservoir volume (Gale et al., 2014; Hoek and Martin, 2014; Weng, 2015). We use sorbing CO_2 (purity of 99.995%) and effectively- non-sorbing He (99.999%) as contrasting permeants for the permeability measurement.

2.2. Apparatus

A standard triaxial apparatus, as shown in Fig. 1, is used as the pressurized core holder. The proppant-sandwiching sample is packed with tape then jacketed in a Viton rubber jacket to seal and isolate the sample from the confining fluid in the core holder. This assembly is then placed in the triaxial core holder (Temco) where both confining and axial stresses to 25 MPa are applied by syringe pumps (ISCO 500D) to a resolution of ± 0.007 MPa. The axial stress is transmitted directly onto both ends of the sample through the platens which connect flow lines to fluid distributors. The end-platens are plumbed to two stainless steel gas reservoirs through tubing and isolating valves at both upstream and downstream extents of the sample. Reservoir volumes are 26.7 ml for the upstream and 16.8 ml for the downstream with reservoir pressures measured by transducers (Omega PX302-2KGV and Omega PX302-5KGV) to resolutions of ± 0.03 MPa. Each transducer is calibrated for each new sample with National Instruments Labview used for data acquisition and pump control.

2.3. Procedure

We use standard pressure transient (pulse) methods for permeability measurements. Once the sample is in the core holder, the system is first evacuated for one hour and then saturated with the desired gas (CO_2 or He). Then, a pressure difference (pulse) is applied between upstream and downstream and its upstream decay and downstream build-up behaviour is recorded and analysed to obtain the permeability (Wang et al., 2011). The tests are performed at both room temperature (23 °C) and supercritical temperature (45 °C) in a water bath, as shown in Fig. 2. Interior gas pressures in the range 2 to 13 MPa access the various phase states of CO_2.

We measure the permeabilities alternately with CO_2 and then He in the same sample to evaluate the impact of the gas on permeability and its recovery/loss after swelling. Then, a comprehensive analysis is performed for the quantitative description of swelling and embedment. As a part of the standard pulse decay method, the permeability is calculated as (Brace et al., 1968),

$$k = \frac{\alpha\mu\beta L V_{up} V_{dn}}{A(V_{up} + V_{dn})} \quad (1)$$

where α is the slope of pressure decay against the logarithm of time; μ and β are the viscosity and compressibility of the fluid, respectively; L is the length of the sample; V_{up} and V_{dn} are volumes of the upstream and downstream reservoirs, respectively; and A is the fluid flow cross-section area in fracture (permeation through the rock matrix is ignored).

The cross-sectional area A is calculated from the average particle diameter and is considered constant for all testing samples. The compressibility of the fluid β is calculated from the bulk modulus

$$\beta = \frac{1}{B_M} = \frac{1}{\upsilon^2 \rho} \quad (2)$$

where B_M is the bulk modulus of the fluid; υ is the speed of sound in the fluid; and ρ is the fluid density.

The values of υ and ρ are recovered from standard characterizations (National Institute of Standards and Technology (NIST)), as shown in Fig. 3. The density and speed of sound in He increase linearly versus pressure with small slopes, although those properties for CO_2 increase or decrease gradually then jump or fall sharply around the phase change pressure. The properties of CO_2 then vary more continuously with pressure at 45 °C than those at 23 °C. Both decline at high temperature, especially under high pressure.

3. Results

A total of five groups of permeability measurements are conducted with multiple repeats in each of these five groups. Each probing injection (increasing gas pressure) and depletion (decreasing gas pressure) are repeated at least three times. The measurements are for CO_2 as gaseous, liquid then supercritical states. The permeabilities for the granite sample are used as a reference where neither embedment nor swelling may occur. Shale sample A was used for multi-purpose testing with repeat tests with He used on samples B, C and D to measure the permeability recovery after CO_2-induced swelling and corresponding embedment. The experimental matrix is shown in Table 1.

3.1. General testing results

Permeability evolutions in granite and shale (sample A) are shown in Fig. 4. Generally, the granite has the largest permeability followed by the “shale + He” case, in which approximately half of the permeability

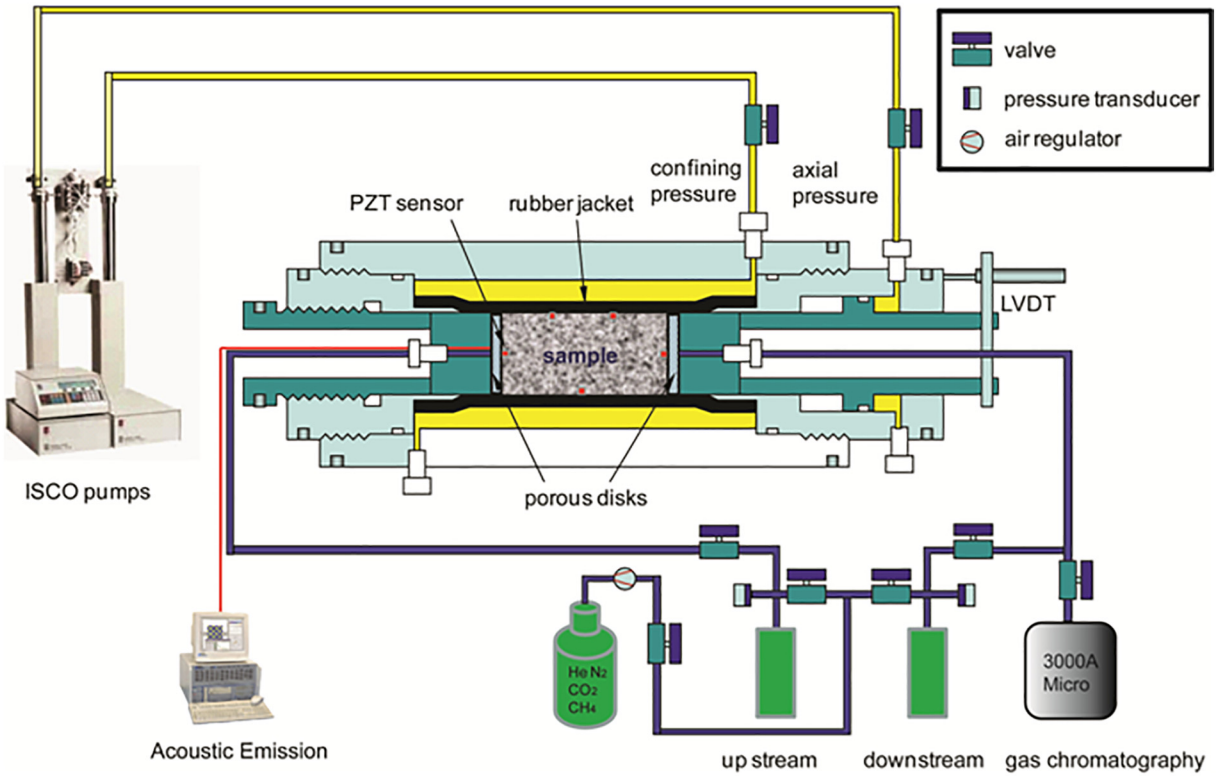

Fig. 1. Schematic of the experimental apparatus (Wang et al., 2011).

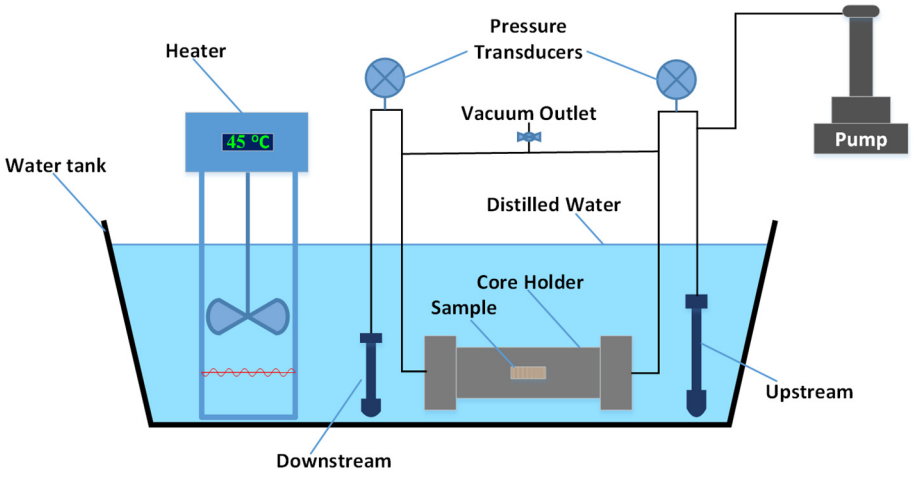

Fig. 2. Schematic of water tank heating system.

is consumed by the embedment. The lowest permeability is obtained for the case of liquid CO_2. Positive linear relationships between increasing gas pressure and increasing permeability are found in those cases.

Swelling and more significant corresponding embedment diminish the permeability significantly for infiltration with gaseous CO_2. A typical U-shaped curve results due to the competition between adsorption (low pressure limit) and effective stress (high gas pressure limit). The permeability relation is a minimum at approximately double the Langmuir pressure of ~5 MPa in this case. The dramatic drop at ~7 MPa has been explained by the sudden volume change during the phase transition of the CO_2 for a relatively stable pressure (Li et al., 2017). For both gaseous and liquid CO_2, the permeabilities remain continuous for overlapping pressures in the range ~ 7 to 9 MPa.

3.2. Permeability recovery behaviour

Repeat experiments on shale samples B, C and D reveal the permeability recovery behaviour following swelling. The permeability returns to ~50 to 70% of the initial value in the repeated He test after injecting CO_2 and shows a parallel linear trend with the prior measurements, as shown in Fig. 5. It is worth noting that the recovery period is relatively short. A comparative trial over different recovery periods (hours and days) yielded similar results. In these tests, the system is evacuated for at least one hour to ensure the complete recovery of swelling.

The three separate groups of the experiments present relatively good repeatability in both values of permeability and trends with pressure and gas state. A minor difference in the repeated He permeability measurement is found in sample D, where the operating

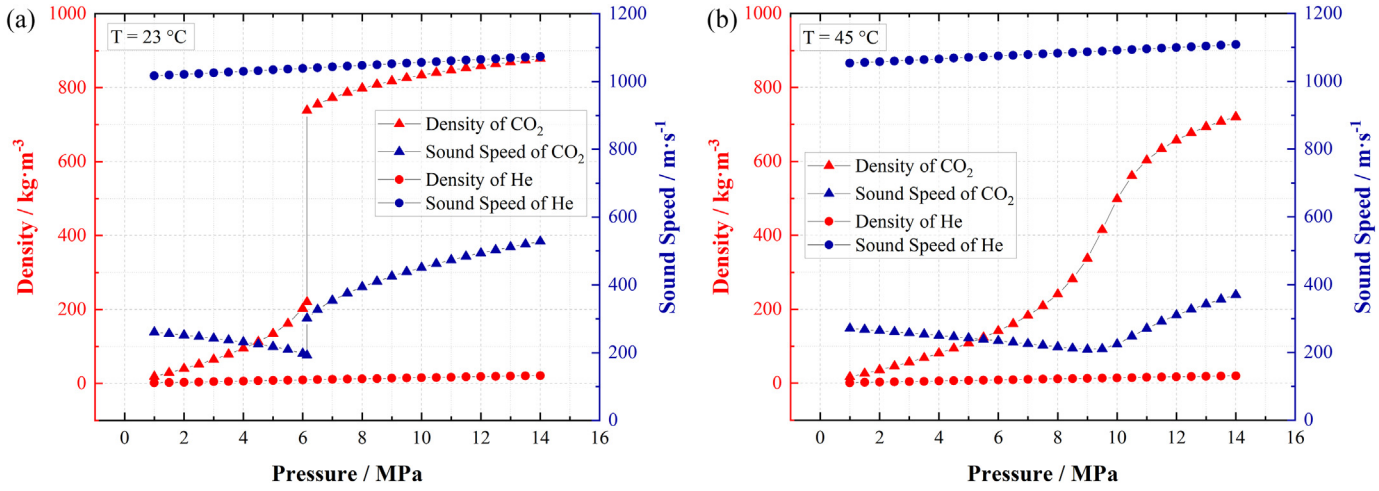

Fig. 3. Density and speed of sound in CO_2 and He (NIST database).

Table 1
Matrix of experiments defining samples and conditions.

Sample Type & No.	Westerly Granite	Greenriver Shale			
		A	B	C	D
Dimensions	25 * 50 mm				
Proppant	Carbo-Lite Ceramisite; 40/80 Mesh (D = 0.177–0.400 mm)				
Gas	Helium	Helium & Carbon Dioxide			
Confining & axial pressure	25 MPa				
Injection pressure	3–9 MPa	3–13 MPa	2–9 MPa	2–13 MPa	2–10 MPa
Temperature	23 °C				45 °C

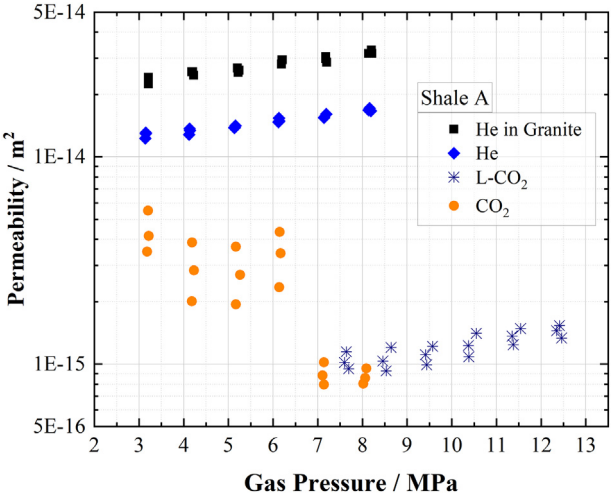

Fig. 4. Permeability evolution versus gas pressure in granite and in shale sample A with injection of He, CO_2 (gaseous) and liquid CO_2 (L-CO_2). The temperature is 23 °C.

temperature is 45 °C and CO_2 exists in a supercritical state. Nearly 70% of the permeability is restored, an increase of ~20% when compared with the cases for gaseous CO_2. Moreover, a W-shaped curve is apparent for supercritical CO_2, which is in accordance with observations on intact specimens of coal (Zhi et al., 2019) - explained by the synthetic effect of phase transition around the critical point and the plasticization of the solid material by supercritical CO_2.

4. Discussion

The flow mechanism determines the linear or U-shaped form of the permeability curve in Fig. 5. Fracture flow, as shown in Fig. 6 (a), is the governing mechanism controlling the permeability evolution in non-sorbing He cases. The particle rearrangement by the various effective stresses reforms the particle interval (from w_0 to w_1), thus approaching the response of parallel plate flow within a fracture. In contrast, the swelling in sorbing CO_2 cases contracts the fracture cross-sectional flow area by Δb, as shown in Fig. 6 (b). The softened rock matrix results in more severe embedment and shrinks the flow path to a residual effective aperture of b_1. The competition between effective stress and swelling dominates the U-shaped curve in Fig. 5. Fig. 6 (c) shows embedment for repeated He replacement after injection of CO_2. We quantitatively distinguish swelling and embedment by contrast calculations (between line 1, 2 and 3) based on the assumption that swelling is reversible and embedment is irreversible.

4.1. Quantification of embedment

For steady parallel plate flow in fractures separated by a constant aperture, the evolution of fracture permeability follows the evolution of fracture aperture (Elsworth and Goodman, 1986; J. Liu et al., 1997; Piggott and Elsworth, 1993). The permeability is proportional to the third power of fracture aperture

$$\frac{K_0}{K_1} = \left(\frac{b_0}{b_1}\right)^3 \tag{3}$$

where K_0 is the initial permeability; K_1 is the diminished permeability; b_0 is the initial aperture; and b_1 is the residual aperture.

Experiments on fractures in granite (neither embedment nor swelling occurs) are used as a reference, in which the aperture ($b_{Granite}$) is equal to the monolayer proppant diameter (the particle deformation is negligible). Then, the residual aperture ($b_{He\text{-}shale}$) after embedment for the non-swelling and embedment-only (He) case is calculated from the relative apertures recovered from Eq. 3 for the non-embedment ($b_{Granite}$) and embedment ($b_{He\text{-}shale}$) cases, as,

$$b_{He-shale} = b_{Granite}\sqrt[3]{\frac{K_{He-shale}}{K_{Granite}}} \tag{4}$$

The embedment depth (($(b_0\text{-}b_1)/2$ in Fig. 6 (a)) is obtained from

$$Embedment = \frac{(b_{Granite} - b_{He-shale})}{2} \tag{5}$$

Similarly, the aperture change for CO_2 includes the additive effects

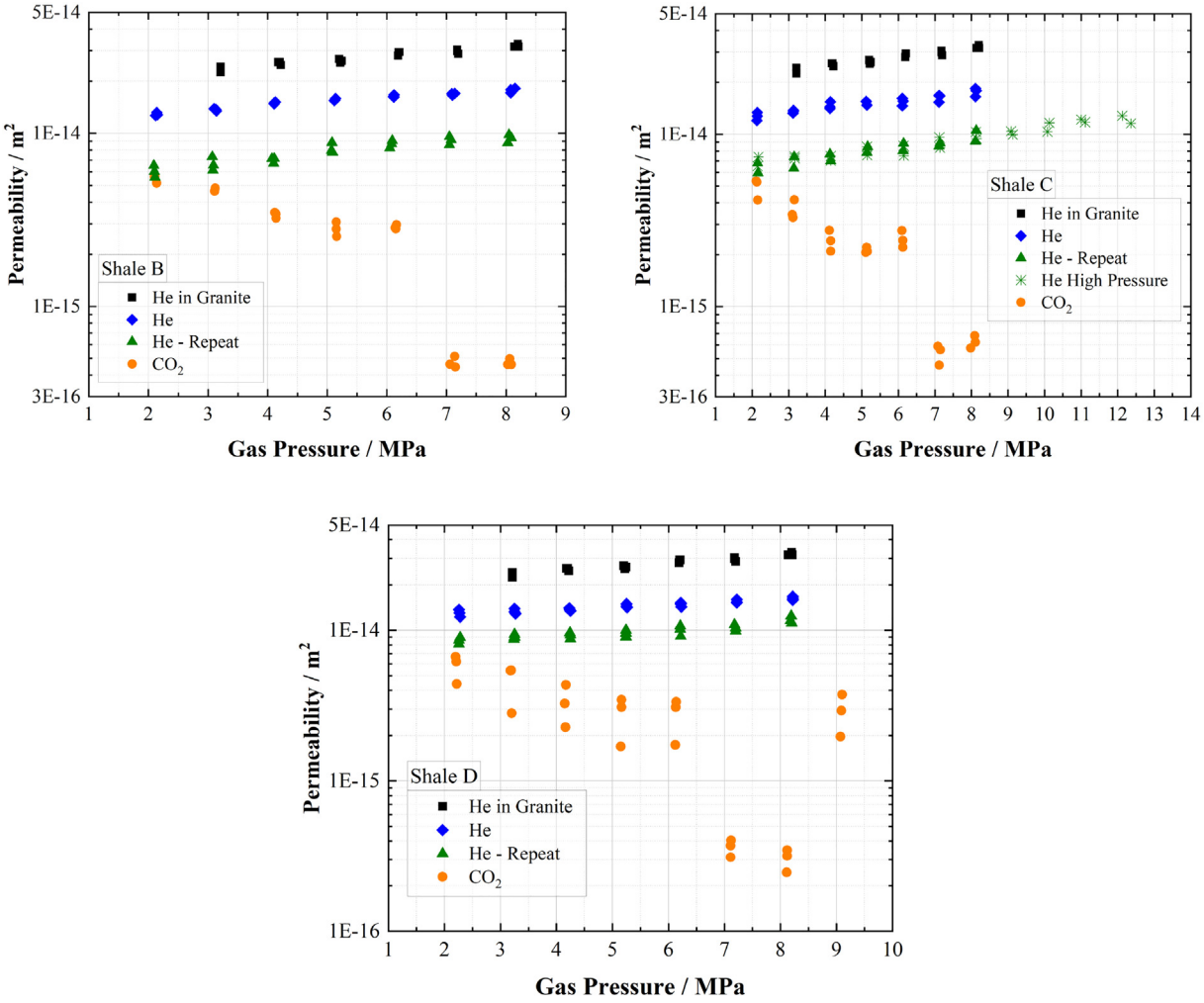

Fig. 5. Permeability evolution in samples B, C and D. The experimental temperatures are 23 °C for samples B and C and 45 °C for sample D. The "He - Repeat" represents He permeability after injecting CO_2. The "He High Pressure" response is to verify testing consistency under higher pressure condition.

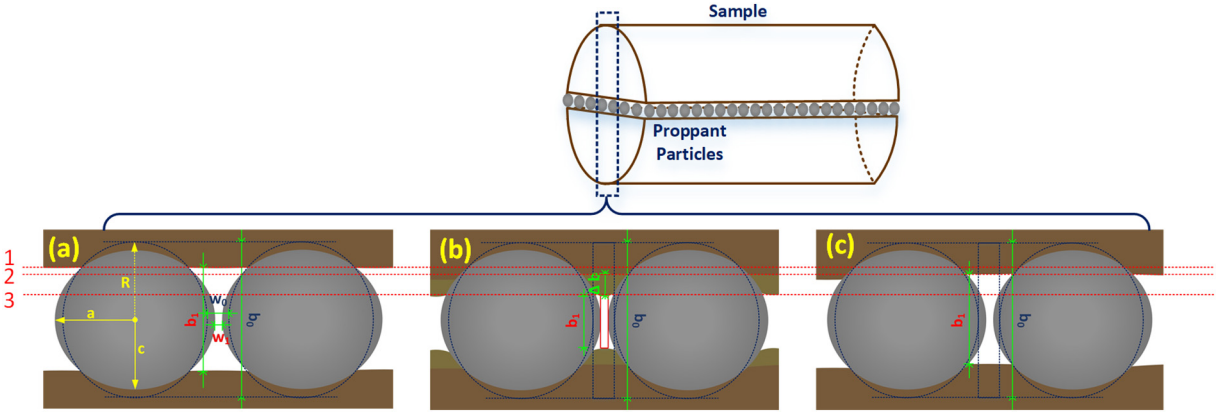

Fig. 6. Schematic of the flowing mechanisms for a propped fracture in shale. (a) initial non-sorbing case; (b) sorbing case; (c) repeated non-sorbing case after injection of sorbing gas.

of embedment and swelling, and is evaluated from,

$$\begin{cases} b_{CO_2-shale} = b_{Granite}\sqrt[3]{\dfrac{K_{CO_2-shale}}{K_{Granite}}} \\ Embedment + Swelling = \dfrac{(b_{Granite} - b_{CO_2-shale})}{2} \end{cases} \quad (6)$$

Eqs. 4 and 6 enable embedment and swelling-penetration depths to be evaluated from the permeability measurements, alone – for the shale fractures. The embedment and swelling depths are plotted in Fig. 7. In general, the embedment and swelling depths vary between 0.02 and 0.11 mm. Similar magnitudes of embedment have been recovered from morphological measurements (Kumar et al., 2015; Li et al., 2017), reportedly in the range 0.03 to 0.09 mm. The slight discrepancy between these results from the larger range of confining pressures used in this

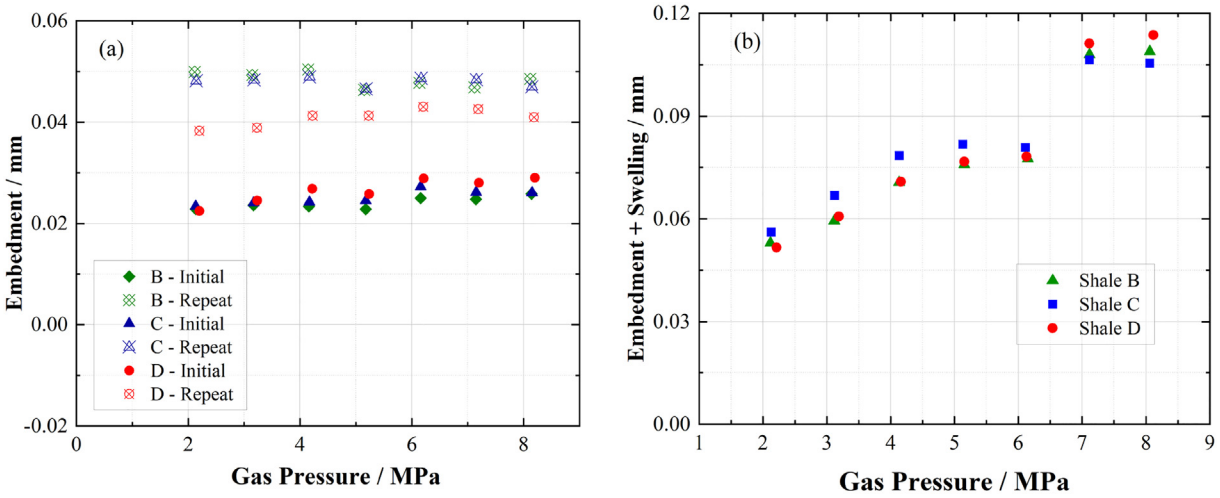

Fig. 7. Embedment and swelling during permeation by He and CO_2. (a) Embedment for non-swelling He; (b) Embedment and swelling for swelling CO_2.

study and the recovery of swelling, occasioned when confinement is removed.

The embedment curves for He are near constant with gas pressure and fluctuate only within a small range since embedment is irreversible. The gas pressure only slightly affects the permeability by particle rearrangement under various effective stresses. The high repeatability of the embedment results are shown for both He and CO_2 cases. The gap between the initial and repeat He tests, with averaged values of 0.025 mm and 0.048 mm, results from irrecoverable embedment induced by swelling after the injection of CO_2 (the difference between line 1 and line 2 in Fig. 6 (a) and (c)). This phenomenon is the least in Shale D test with an average repeat embedment value of 0.041 mm, where the CO_2 is supercritical. In this case, sorption of CO_2 dominates over embedment, which is influenced by the gas pressure following Langmuir adsorption. The embedment depth scales linearly with gas pressure, as shown in Fig. 7 (b). With the addition of swelling, the aperture reduces 0.053 to 0.108 mm ($(b_0\text{-}b_1)/2$ in Fig. 6 (b)) as a result of injection of CO_2.

4.2. Swelling analysis accommodating the Langmuir equation

We quantitatively distinguish between embedment and swelling by contrasting response for these two cases – embedment with He and the additive effects of embedment and swelling with CO_2. Swelling-related embedment depth (Δb as shown in Fig. 6 (b)) is equal to the difference in aperture reduction between CO_2 and the repeat He tests (the difference between line 2 and line 3 in Fig. 6 (b) and (c)), according to the assumption that swelling is reversible and embedment is irreversible. Thus,

$$Swelling = (Embedment + Swelling)_{CO_2} - Embedment_{He-repeat} \tag{7}$$

then, the fractional adsorption may be calculated from the Langmuir isothermal adsorption relation that defines swelling-related embedment. The Langmuir relation is,

$$\omega = \frac{V}{V_L} = \frac{P}{P_L + P} \tag{8}$$

where ω is the fractional adsorption; V is the adsorbed volume; V_L is the Langmuir volume; P is the injection pressure; P_L is the Langmuir pressure and is 2.5 MPa under the experimental conditions of this study.

Embedment for the case of He is calibrated independently from the particle deformation. The deformation γ is calculated for an elastic model as (Kewen Li and Lyu, 2015; White et al., 2019).

$$\gamma = 1.04D\left(m^2 P_{eff}\frac{1-\nu^2}{E}\right)^{2/3} \tag{9}$$

where γ is the vertical deformation ("c" direction in Fig. 6 (a)); D is the particle diameter; m is the particle interval coefficient ($m = 1$ when particles are uniformly displaced); P_{eff} is effective pressure applied to the particle; ν and E are Poisson Ratio and Young's Modulus of the particle. Selected parameter values and units are shown in Table 2.

Correcting for the reduction in proppant diameter γ due to applied stress, yields a corrected final magnitude of embedment (Fig. 8). This effect of proppant deformation is of the order of 0.001 mm and is two orders of magnitude less than the embedment for CO_2. We use this calibration to improve accuracy.

The swelling, its proportion and corresponding fractional adsorption are calculated by Eq. 7 and Eq. 8, and plotted in Fig. 9. In general, relatively good repeatability of the measurement is demonstrated by similar results recovered from the three groups of experiments. Swelling is approximately proportional to the fractional adsorption (Fig. 9) and ranges from 0.005 to 0.06 mm and contributes 9 to 56% of the total aperture reduction – indicating a significant effect on permeability evolution.

4.3. Calibration equation representing swelling and induced embedment

More common outcomes are generated by fitting the relation between aperture reduction ratio and fractional adsorption. Aperture reduction (AR) is defined as half of the aperture change ($(b_0\text{-}b_1)/2$ as shown in Fig. 6), due to both embedment and swelling. This is evaluated from Eq. 5 for the case of non-sorbing He and from Eq. 6 for sorbing CO_2.

As shown in Fig. 10 (a), swelling increases embedment by a factor of 1.84 to 1.93 between the He permeability experiments. For CO_2, a power-law relation is apparent between fractional adsorption and aperture reduction (Fig. 10 (b)) as conditioned by the choice of Eq. 6. The aperture reduction ratio is unity when fractional adsorption is zero, as implied by the absence of swelling. By fixing this intercept (the Point (0, 1) in Fig. 10 (b)), the aperture reduction can be calibrated to the empirical equation,

Table 2
Calculation parameters and values.

D / mm	m	ν	E / GPa
0.2884	1	0.2	34.47

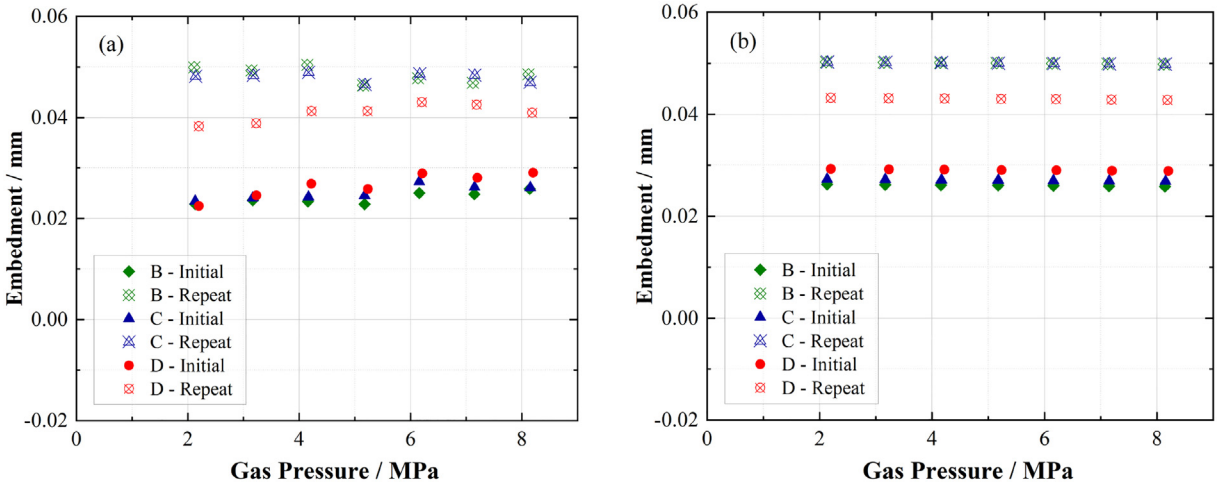

Fig. 8. Embedment relative to gas pressure for He. (a) Original data; (b) Proppant deformation calibrated data.

$$\frac{AR_1}{AR_0} = e^{1.724\omega} = e^{1.724\frac{P}{P_L+P}} \tag{10}$$

where the AR_1 is the calibrated aperture reduction ($(b_0\text{-}b_1)/2$ as shown in Fig. 6 (b)) involving both embedment and swelling and AR_0 is the initial aperture reduction ($(b_0\text{-}b_1)/2$ as shown in Fig. 6 (a)) neglecting the swelling effect. The value of AR_1 accommodates the swelling effect and updates the prediction of the permeability in propped fractures.

4.4. Verification

An indirect method is proposed to examine the universal applicability of Eq. 10 – since few direct measurements of embedment and swelling are available. Permeability is the target parameter for the verification. The correlation between effective aperture and permeability is simplified to a cubic power-law relation as

$$K = \theta b_{eff}^3 \tag{11}$$

where θ is the coefficient of the aperture-permeability correlation and is obtained through trial and error; b_{eff} is the effective aperture and is an intermediate variable calculated from Eq. 3.

In this study, we fit the cubic relation between permeability and effective aperture in Fig. 11. A user-defined model ($y = Ax^3$) is used for regression based on the definition of fluid flow cross-sectional area (A) in Eq. 1, where flow in the rock matrix is ignored. The fitted coefficient (θ) is 1109, which can be used as a reference or comparison for trial and error verification.

Then, the non-sorbing gas permeability is applied to predict the permeability for the sorbing gas case by the following relations,

$$AR = (D - b_{eff})/2 = \left(D - \sqrt[3]{\frac{K}{\theta}}\right)/2 \tag{12}$$

$$\frac{AR_1}{AR_0} = \frac{\theta D - \sqrt[3]{\theta^2 K_1}}{\theta D - \sqrt[3]{\theta^2 K_0}} = e^{1.724\frac{P}{P_L+P}} \tag{13}$$

where D is the average particle diameter; K_1 is the predicted permeability for the case of sorbing gas; K_0 is the measured permeability for the case of non-sorbing gas, recovered from the corresponding series of experiments.

Prior experimental results are available with different rock types and for different gases (Kumar et al., 2015; Li et al., 2017), including coal (with injection of CO_2) and CH_4 (in a propped shale sample). For coal, 70–140 mesh proppant was used, with an average diameter of 0.159 mm and a Langmuir pressure of ~1.75 MPa. For shale with CH_4, the corresponding average diameter and Langmuir pressure are 0.288 mm and 3.5 MPa, respectively. The optimized coefficients (θ) obtained by trial and error, are 280 for CH_4 (shale) and 2250 for coal (CO_2), respectively, with results shown in Fig. 12. Apparently, the predictions fit the measurements and exhibit similar trends with gas pressure. The MRD (mean relative deviation) and MAD (mean absolute deviation) are −3.57% and 9.22% for the prediction for CH_4 in shale

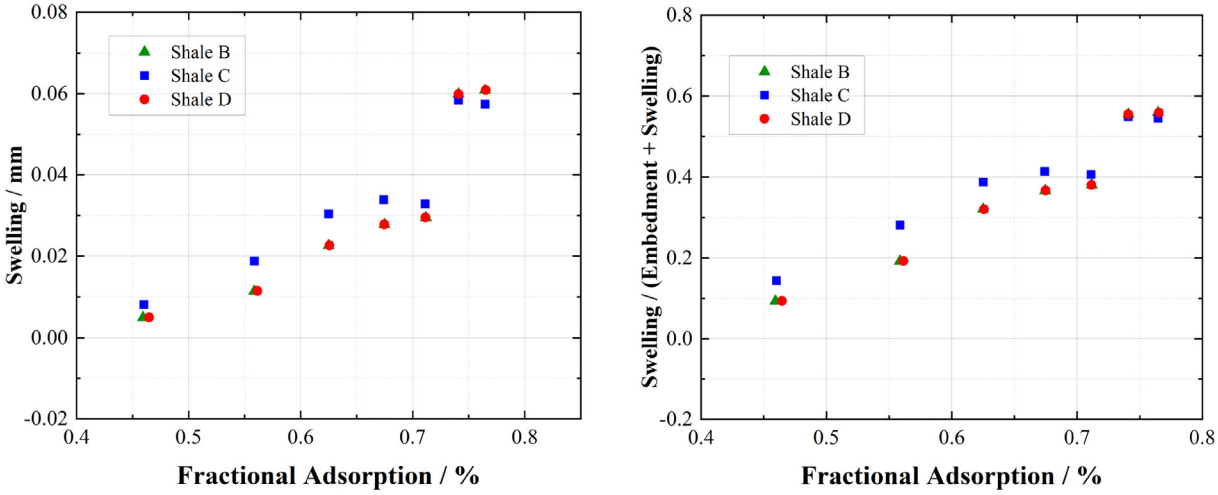

Fig. 9. Evolution of swelling and its proportion relative to fractional adsorption for CO_2.

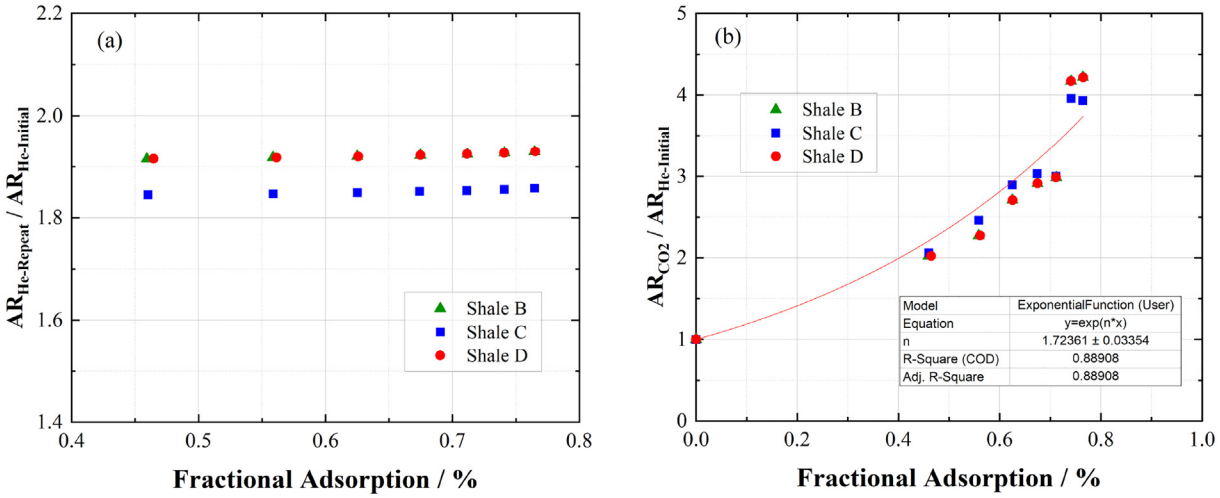

Fig. 10. Aperture reduction (AR) ratio between initial and repeat applications of gas versus fractional adsorption for (a) He and for (b) CO_2.

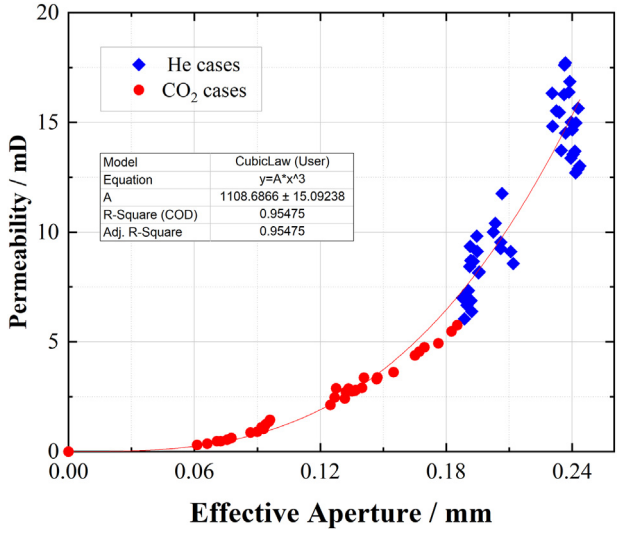

Fig. 11. The cubic power-law relation fit to permeability versus effective aperture for all cases.

and − 4.50% and 7.06% for CO_2 in coal.

5. Conclusions

Permeability evolution in propped shale fractures to non-adsorptive He and adsorptive CO_2 have been measured. Embedment and swelling depth have been evaluated by using rigid split samples of granite as an example where no embedment can occur. Further analyses have included comparisons between non-adsorptive gases and adsorptive gas utilizing the Langmuir isotherm to define swelling and embedment effects. The main observations of this work are as follow:

(1) Permeability evolution is linear with pressure for non-sorbing He, U-shaped for sorbing CO_2 (gaseous) and W-shaped curve for supercritical CO_2. One exception is for liquid CO_2, which forms a linear curve with the lowest permeability. The competition between injection pressure (changing the effective stress) and swelling and the phase state transformation are the main factors controlling these forms of permeability evolution for the case of CO_2.
(2) Permeability evolution is linear in pressure for both initial and repeated He injection, with the intervening injection of CO_2 – but parallel and offset. Approximately ~50–70% of the permeability recovers from the recovery of swelling after the desorption of CO_2, in which supercritical CO_2 increases the permeability recovery by

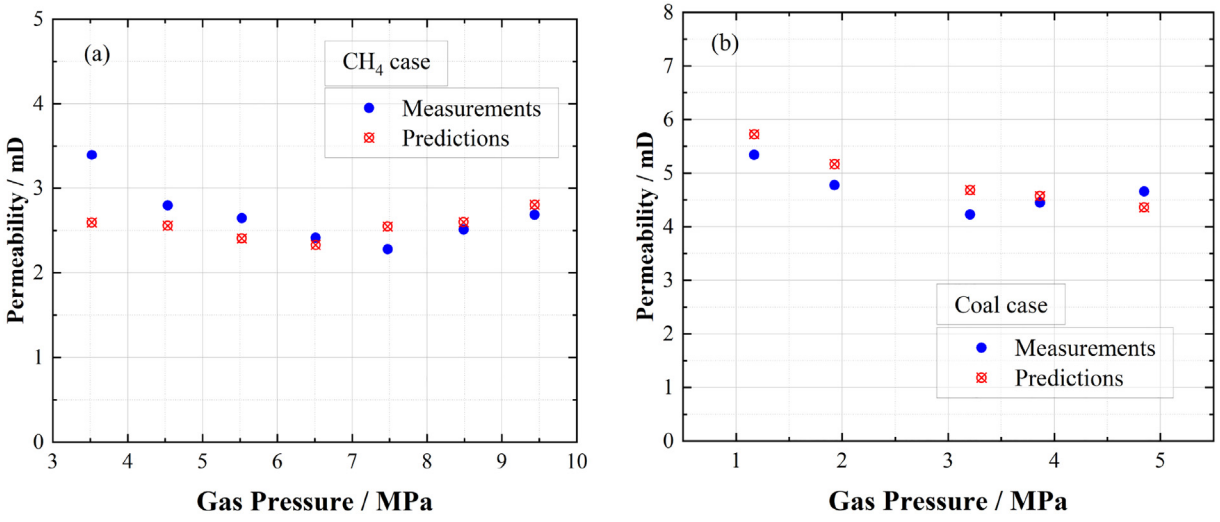

Fig. 12. Permeability prediction and comparison for (a) CH_4 case and (b) Coal case.

~20% when compared with the case for gaseous CO_2.

(3) Embedment depth is 0.025 to 0.048 mm for permeation of He, while swelling increases the embedment by a factor of ~1.84–1.93 between the initial and repeated He tests. The swelling and induced embedment, for CO_2, varies between 0.053 and 0.108 mm where the swelling depth contributes 0.005 to 0.06 mm, representing 9 to 56% of the total aperture reduction relative to the adsorbed mass. These depths are approximately proportional to the gas pressure and fractional adsorption for the case of CO_2, and near constant for He.

(4) A new calibration equation representing swelling and induced embedment is generated accommodating Langmuir isothermal sorption and verified against prior experiments with different rock types (coal) and for different sorbing gases (CH_4). It provides an improved method for predicting fracture conductivity related to enhanced gas recovery, and also benefits the understanding of CO_2 sealing behaviour and long-term migration, thus improving the evaluation of CO_2 storage capacity and security.

Acknowledgements

This research has received funding from the European Union's Horizon 2020 research and innovation programme under the Marie Sklodowska-Curie grant agreement No. 846775.

References

Arshadi, M., Zolfaghari, A., Piri, M., Al-Muntasheri, G.A., Sayed, M., 2017. The effect of deformation on two-phase flow through proppant-packed fractured shale samples: a micro-scale experimental investigation. Adv. Water Resour. 105, 108–131. https://doi.org/10.1016/j.advwatres.2017.04.022.

Bandara, K.M.A.S., Ranjith, P.G., Rathnaweera, T.D., 2019. Improved understanding of proppant embedment behavior under reservoir conditions: a review study. Powder Technol. 352, 170–192. https://doi.org/10.1016/j.powtec.2019.04.033.

Bielicki, J.M., Langenfeld, J.K., Tao, Z., Middleton, R.S., Menefee, A.H., Clarens, A.F., 2018. The geospatial and economic viability of CO 2 storage in hydrocarbon depleted fractured shale formations. International Journal of Greenhouse Gas Control 75, 8–23. https://doi.org/10.1016/j.ijggc.2018.05.015.

Brace, W.F., Walsh, J.B., Frangos, W.T., 1968. Permeability of granite under high pressure. J. Geophys. Res. 73 (6), 2225–2236. https://doi.org/10.1029/JB073i006p02225.

Buscheck, T.A., White, J.A., Carroll, S.A., Bielicki, J.M., Aines, R.D., 2016. Managing geologic CO2 storage with pre-injection brine production: a strategy evaluated with a model of CO2 injection at Snøhvit. Energy Environ. Sci. 9 (4), 1504–1512. https://doi.org/10.1039/c5ee03648h.

Elsworth, D., Goodman, R.E., 1986. Characterization of rock fissure hydraulic conductivity using idealized wall roughness profiles. Int. J. Rock Mech. Min. Sci. Geomech. Abstr. 23 (3), 233–243.

Gale, J.F.W., Laubach, S.E., Olson, J.E., Eichhuble, P., Fall, A., 2014. Natural Fractures in shale: a review and new observations. AAPG Bull. 98 (11), 2165–2216. https://doi.org/10.1306/08121413151.

Hoek, E., Martin, C.D., 2014. Fracture initiation and propagation in intact rock – a review. J. Rock Mech. Geotech. Eng. 6 (4), 287–300. https://doi.org/10.1016/j.jrmge.2014.06.001.

Kewen Li, Y.G., Lyu, Youchang, 2015. New mathematical models for calculating proppant embedment and fracture conductivity. SPE J. 20 (3), 1–12.

Kolster, C., Masnadi, M.S., Krevor, S., Mac Dowell, N., Brandt, A.R., 2017. CO2 enhanced oil recovery: a catalyst for gigatonne-scale carbon capture and storage deployment? Energy Environ. Sci. 10 (12), 2594–2608. https://doi.org/10.1039/c7ee02102j.

Kumar, H., Elsworth, D., Liu, J., Pone, D., Mathews, J.P., 2015. Permeability evolution of propped artificial fractures in coal on injection of CO2. J. Pet. Sci. Eng. 133, 695–704. https://doi.org/10.1016/j.petrol.2015.07.008.

Li, X., Feng, Z., Han, G., Elsworth, D., Marone, C., Saffer, D., Cheon, D.-S., 2017. Permeability Evolution of Propped Artificial Fractures in Green River Shale. Rock Mech. Rock. Eng. 50 (6), 1473–1485. https://doi.org/10.1007/s00603-017-1186-2.

Liu, H., Wang, F., Zhang, J., Meng, S., Duan, Y., 2014. Fracturing with carbon dioxide: Application status and development trend. Pet. Explor. Dev. 41 (4), 513–519. https://doi.org/10.1016/s1876-3804(14)60060-4.

Liu, H.-H., Rutqvist, J., 2009. A New Coal-Permeability Model: Internal Swelling stress and Fracture–Matrix Interaction. Transp. Porous Media 82 (1), 157–171. https://doi.org/10.1007/s11242-009-9442-x.

Liu, J., Elsworth, D., & Brady, B. H. (1997). Analytical evaluation of post-excavation hydraulic conductivity field around a tunnel. *International Journal of Rock Mechanics and Mining Sciences, 23*(3-4), 181.e181-181.e187.

Mazumder, S., Wolf, K.H., 2008. Differential swelling and permeability change of coal in response to CO2 injection for ECBM. Int. J. Coal Geol. 74 (2), 123–138. https://doi.org/10.1016/j.coal.2007.11.001.

Middleton, R.S., Carey, J.W., Currier, R.P., Hyman, J.D., Kang, Q., Karra, S., ... Viswanathan, H.S., 2015. Shale gas and non-aqueous fracturing fluids: Opportunities and challenges for supercritical CO2. Applied Energy 147, 500–509. https://doi.org/10.1016/j.apenergy.2015.03.023.

Piggott, A.R., Elsworth, D., 1993. Laboratory assessment of the equivalent apertures of a rock fracture. Geophys. Res. Lett. 20 (13), 1387–1390.

Santos, L., Dahi Taleghani, A., Li, G., 2018. Expandable proppants to moderate production drop in hydraulically fractured wells. Journal of Natural Gas Science and Engineering 55, 182–190. https://doi.org/10.1016/j.jngse.2018.04.026.

Tang, Y., Ranjith, P.G., 2018. An experimental and analytical study of the effects of shear displacement, fluid type, joint roughness, shear strength, friction angle and dilation angle on proppant embedment development in tight gas sandstone reservoirs. Int. J. Rock Mech. Min. Sci. 107, 94–109. https://doi.org/10.1016/j.ijrmms.2018.03.008.

Tayari, F., Blumsack, S., 2020. A real options approach to production and injection timing under uncertainty for CO2 sequestration in depleted shale gas reservoirs. Appl. Energy *263*. https://doi.org/10.1016/j.apenergy.2020.114491.

Wang, S., Elsworth, D., Liu, J., 2011. Permeability evolution in fractured coal: the roles of fracture geometry and water-content. Int. J. Coal Geol. 87 (1), 13–25. https://doi.org/10.1016/j.coal.2011.04.009.

Wang, S., Elsworth, D., Liu, J., 2013. Permeability evolution during progressive deformation of intact coal and implications for instability in underground coal seams. Int. J. Rock Mech. Min. Sci. 58, 34–45. https://doi.org/10.1016/j.ijrmms.2012.09.005.

Wang, S., Feng, Q., Javadpour, F., Xia, T., Li, Z., 2015. Oil adsorption in shale nanopores and its effect on recoverable oil-in-place. Int. J. Coal Geol. 147–148, 9–24. https://doi.org/10.1016/j.coal.2015.06.002.

Wen, Q., Zhang, S., Wang, L., Liu, Y., Li, X., 2007. The effect of proppant embedment upon the long-term conductivity of fractures. J. Pet. Sci. Eng. 55 (3–4), 221–227. https://doi.org/10.1016/j.petrol.2006.08.010.

Weng, X., 2015. Modeling of complex hydraulic fractures in naturally fractured formation. Journal of Unconventional Oil and Gas Resources 9, 114–135. https://doi.org/10.1016/j.juogr.2014.07.001.

White, B.W., Jordan, J.L., Spowart, J.E., Thadhani, N.N., 2019. Particle strain analysis of epoxy-based composites following quasi-static and dynamic compression. Journal of Dynamic Behavior of Materials 5 (1), 24–38. https://doi.org/10.1007/s40870-019-00182-2.

Zhang, J., Hou, J., 2016. Theoretical conductivity analysis of surface modification agent treated proppant II – Channel fracturing application. Fuel 165, 28–32. https://doi.org/10.1016/j.fuel.2015.10.026.

Zhang, J., Ouyang, L., Zhu, D., Hill, A.D., 2015. Experimental and numerical studies of reduced fracture conductivity due to proppant embedment in the shale reservoir. J. Pet. Sci. Eng. 130, 37–45. https://doi.org/10.1016/j.petrol.2015.04.004.

Zhang, X., Lu, Y., Tang, J., Zhou, Z., Liao, Y., 2017. Experimental study on fracture initiation and propagation in shale using supercritical carbon dioxide fracturing. Fuel 190, 370–378. https://doi.org/10.1016/j.fuel.2016.10.120.

Zhang, X., Ranjith, P.G., Lu, Y., Ranathunga, A.S., 2019. Experimental investigation of the influence of CO2 and water adsorption on mechanics of coal under confining pressure. Int. J. Coal Geol. 209, 117–129. https://doi.org/10.1016/j.coal.2019.04.004.

Zhi, S., Elsworth, D., Liu, L., 2019. W-shaped permeability evolution of coal with supercritical CO2 phase transition. Int. J. Coal Geol. 211, 1–14. https://doi.org/10.1016/j.coal.2019.103221.